The Astrophysical Journal Letters, 765:L35 (6pp), 2013 March 10 doi:10.1088/2041-8205/765/2/L35

THE GALACTIC CENTER CLOUD G0.253+0.016: A MASSIVE DENSE CLOUD WITH LOW STAR FORMATION POTENTIAL

Jens Kauffmann[1], Thushara Pillai[1,3], and Qizhou Zhang[2]
[1] Astronomy Department, California Institute of Technology, 1200 East California Boulevard, Pasadena, CA 91125, USA; jens.kauffmann@astro.caltech.edu
[2] Harvard-Smithsonian Center for Astrophysics, 60 Garden Street MS78, Cambridge, MA 02138, USA
Received 2012 June 12; accepted 2012 December 25; published 2013 February 22

ABSTRACT

We present the first interferometric molecular line and dust emission maps for the Galactic Center (GC) cloud G0.253+0.016, observed using CARMA and the SMA. This cloud is very dense, and concentrates a mass exceeding the Orion Molecular Cloud Complex ($2 \times 10^5\ M_\odot$) into a radius of only 3 pc, but it is essentially starless. G0.253+0.016 therefore violates "star formation laws" presently used to explain trends in galactic and extragalactic star formation by a factor ∼45. Our observations show a lack of dense cores of significant mass and density, thus explaining the low star formation activity. Instead, cores with low densities and line widths $\lesssim$1 km s^{-1}—probably the narrowest lines reported for the GC region to date—are found. Evolution over several 10^5 yr is needed before more massive cores, and possibly an Arches-like stellar cluster, could form. Given the disruptive dynamics of the GC region, and the potentially unbound nature of G0.253+0.016, it is not clear that this evolution will happen.

Key words: Galaxy: center – ISM: clouds – stars: formation

Online-only material: color figures

1. INTRODUCTION

It is generally understood that the level of ongoing star formation (SF) activity in a cloud correlates with the reservoir of dense gas. This concept first became important for extragalactic research (e.g., Gao & Solomon 2004) and has since been expanded to include the Milky Way (Wu et al. 2010; Lada et al. 2010; Heiderman et al. 2010; Gutermuth et al. 2011). Such work suggests that (1) the mass of dense gas and SF rate are proportional, and that (2) the proportionality constant is the same for all clouds near and far. These are the key results for efforts to understand the Milky Way and extragalactic SF (Kennicutt & Evans 2012).

It is thus interesting to study regions like the Galactic center (GC) molecular cloud G0.253+0.016 (or M0.25+0.01; Guesten et al. 1981), which is more massive and dense than the Orion A cloud (∼$2 \times 10^5\ M_\odot$ in 2.8 pc radius for G0.253+0.016; Lis et al. 1994; Longmore et al. 2012, hereafter L12), but hardly forms stars at all (Lis et al. 1994). An infrared luminosity of the entire cloud of $\leqslant 3 \times 10^5\ L_\odot$, and the absence of embedded compact HII regions in 8.4 GHz Very Large Array maps, imply $\lesssim$5 embedded stars earlier than B0 (Lis et al. 2001). *Spitzer* can provide more stringent limits, as it can detect SF at luminosities of a few $10^3\ L_\odot$ out to distances ≈7 kpc (e.g., in Infrared Dark Clouds, IRDCs; Zhang et al. 2009; Pillai et al. 2011). However, this analysis is beyond the scope of this Letter. A faint H_2O maser has been detected in the cloud (Lis et al. 1994), but no other masers reside in the area (Caswell et al. 2010, 2011). G0.253+0.016 appears to be in a very extreme physical state, with gas kinetic temperatures ∼80 K exceeding dust temperatures $\leqslant$30 K (Guesten et al. 1981; Carey et al. 1998; Lis et al. 2001; L12). G0.253+0.016 forms part of the ∼100 pc circumnuclear ring of clouds (Molinari et al. 2011) at ∼8.5 kpc distance (also see L12).

Dense GC clouds may play a key role in the mysterious formation of compact and massive stellar aggregates like the "Arches" cluster (Lis & Menten 1998; L12). For all of these reasons, we present the first high-resolution interferometric line and dust emission data on G0.253+0.016, obtained using the Combined Array for Research in Millimeter-wave Astronomy (CARMA) and the Submillimeter Array (SMA).

2. OBSERVATIONS AND DATA REDUCTION

The SMA[4] N_2H^+ (3–2; ≈0.34 km s^{-1} resolution) and continuum observations near 280 GHz (4 GHz total bandwidth) were made with seven antennas in compact-north configuration in a single track in 2009 June. Eleven positions separated at less than half a 42″ primary beam were observed. The 345 GHz receiver was tuned to the N_2H^+ line in the lower sideband spectral band s4, using 256 channels per chunk and 24 chunks per sideband. The data were taken under good weather conditions at <1.3 mm water vapor with characteristic system temperatures <180 K.

The CARMA[5] observations were executed in CARMA23 mode in 2011 November in a combined D and SH configuration. Four upper sidebands were used to observe spectral lines (N_2H^+ [1–0], HCO^+ [1–0], SiO [2–1]; ≈0.5 km s^{-1} resolution; HCO^+ is not analyzed here) and continuum (500 MHz bandwidth) for calibration purposes. Six positions, spaced at half the ≈80″ primary beam for the 10.4 m telescopes, were observed. We flagged 3.5 m telescope baselines <50 ns to reduce sidelobes.

[3] CARMA Fellow.

[4] The Submillimeter Array is a joint project between the Smithsonian Astrophysical Observatory and the Academia Sinica Institute of Astronomy and Astrophysics, and is funded by the Smithsonian Institution and the Academia Sinica.

[5] Support for CARMA construction was derived from the Gordon and Betty Moore Foundation, the Kenneth T. and Eileen L. Norris Foundation, the James S. McDonnell Foundation, the Associates of the California Institute of Technology, the University of Chicago, the states of California, Illinois, and Maryland, and the National Science Foundation (NSF). Ongoing CARMA development and operations are supported by the NSF and the CARMA partner universities.

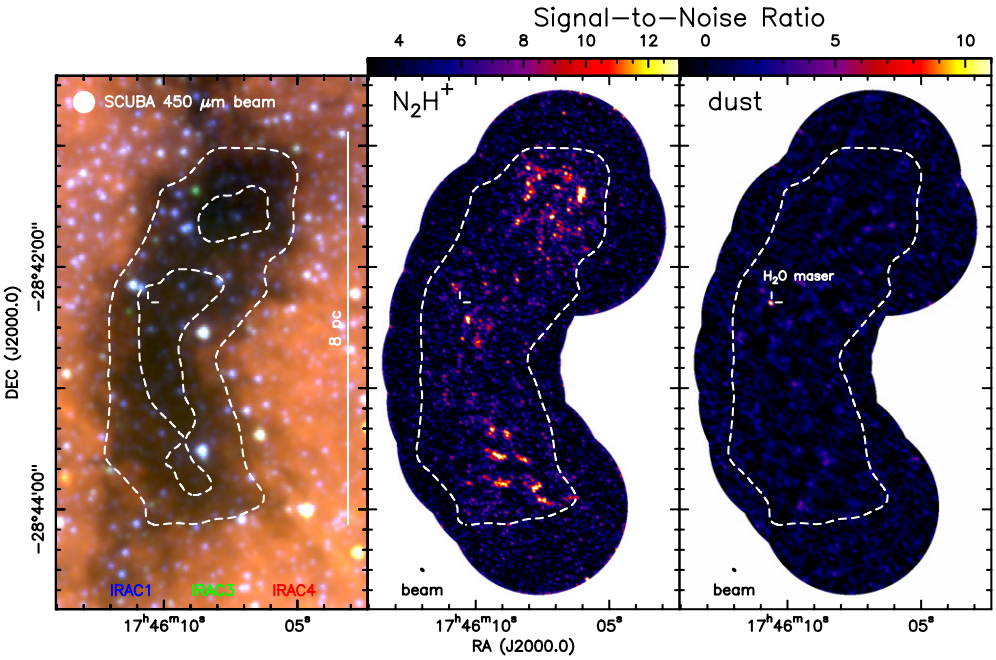

Figure 1. *Spitzer* and SMA maps of G0.253+0.016. The left panel presents *Spitzer* IRAC data. Overlaid are 450 μm wavelength intensity contours at 30 and 70 Jy beam^{-1} (SCUBA Legacy Archive; Di Francesco et al. 2008). The lower contour is repeated in all maps shown. The middle and right panels present signal-to-noise maps of the N_2H^+ (3–2) and 280 GHz dust continuum probed by the SMA. The H_2O maser reported by Lis et al. (1994) is marked.

(A color version of this figure is available in the online journal.)

Calibration and imaging were done using MIR (an IDL-based SMA package), MIRIAD, and GILDAS. Flux calibrations using Titan and Uranus for the SMA, and Neptune for CARMA are expected to be accurate within 20%.

3. RESULTS

3.1. SMA Dust Emission: No Compact Cores

Figure 1 (right) presents the 280 GHz dust emission data, observed with a beam size of 2.″6 × 1.″8 (P.A. = 48°). A continuum peak of 90 mJy beam^{-1} is detected within 0.″5 of the aforementioned H_2O maser position reported by Lis et al. (1994). The remaining part of the map is free of emission above the 5σ noise level of 30 mJy beam^{-1}.

We adopt a dust temperature of 20 K, following *Herschel*-based estimates of 20–25 K (L12), and Ossenkopf & Henning (1994) dust opacities scaled down by a factor 1.5 (0.008 cm^2 g^{-1}; see Kauffmann et al. 2010a and Appendix A of Kauffmann et al. 2008). The 5σ noise level corresponds to an H_2 column density of 1.7×10^{23} cm^{-2}. Toward the H_2O maser, the column density derived from the intensity is 5.2×10^{23} cm^{-2}. This yields masses per beam of $<26\,M_\odot$ and $78\,M_\odot$, respectively, when integrating the column densities over the half power beam width (of 0.046 pc effective radius).

Note that L12 use Ossenkopf & Henning (1994) opacities. For consistency, we increase their *Herschel*-based mass measurement by a factor 1.5.

3.2. SMA N_2H^+ Data: Gas Densities $\leqslant 3 \times 10^5$ cm^{-3}

Figure 1 (middle) summarizes the SMA observations of the N_2H^+ (3–2) line, observed with a beam size of 2.″7 × 1.″9 (P.A. = 46°). It presents a signal-to-noise ratio (S/N) map: at a given location, we divide the signal in the brightest velocity channel by the standard deviation obtained from channels known to be free of emission. Manual inspection reveals emission at velocities from −10 to + 60 km s^{-1}, indicating channels free of emission at velocities 70–100 km s^{-1}. Peak positions with an S/N $\geqslant$ 10 are considered as potentially detected (i.e., 56 positions); detections are deemed reliable for FWHM diameters larger than two beams, permitting lower threshold peak S/Ns $\geqslant$ 8 (22 positions). Figure 1 (middle) illustrates these positions. These spectra are characterized using one-component Gaussian fits. This approach ignores N_2H^+ hyperfine blending, which, however, is considered in the modeling below. Example spectra are shown in Figure 2(a). Manual inspection always reveals one single significant velocity component per position.

We model the N_2H^+ observations from Figure 2(b) using the MOLLIE non-LTE hyperfine radiative transfer code in the hyperfine statistical equilibrium approximation (Keto & Rybicki 2010). We adopt a relative N_2H^+ abundance of 1.5×10^{-10} per H_2 (e.g., Tafalla et al. 2006). Spherical H_2 density profiles $n = n_{0.1\,\mathrm{pc}} \cdot (r/0.1\,\mathrm{pc})^{-2}$ are assumed, with the density vanishing for radii $\geqslant$0.5 pc. The other free parameters, i.e., the non-thermal gas velocity dispersion, $\sigma_{v,\mathrm{in}}$, expressed by intrinsic line widths $\Delta v_{\mathrm{in}} = (8\ \ln[2])^{1/2}\,\sigma_{v,\mathrm{in}}$; and the kinetic temperature, T_{kin}, are assumed to be constant within the model sphere. We adopt $T_{\mathrm{kin}} = 20$ K, based on the L12 dust temperature, resulting in optically thick (3–2) lines. The (1–0) emission is not modeled here; it probes a larger spatial scale which is not focus of this Letter. For a given density, higher abundances or temperatures imply higher intensities.

As shown in Figure 2(b), the brightest N_2H^+ (3–2) peaks can be modeled using densities $n_{0.1\mathrm{pc}} = (2 \pm 1) \times 10^5$ cm^{-3}. Integration of the implied density profiles thus yields masses $(260 \pm 125)\,M_\odot$ within apertures of 0.1 pc projected radius for the most massive structures.

Surprisingly, the continuum-detected H_2O-maser position is not detected in N_2H^+. The H_2O-maser position is probably less abundant in N_2H^+, and thus not detectable, as seen in some

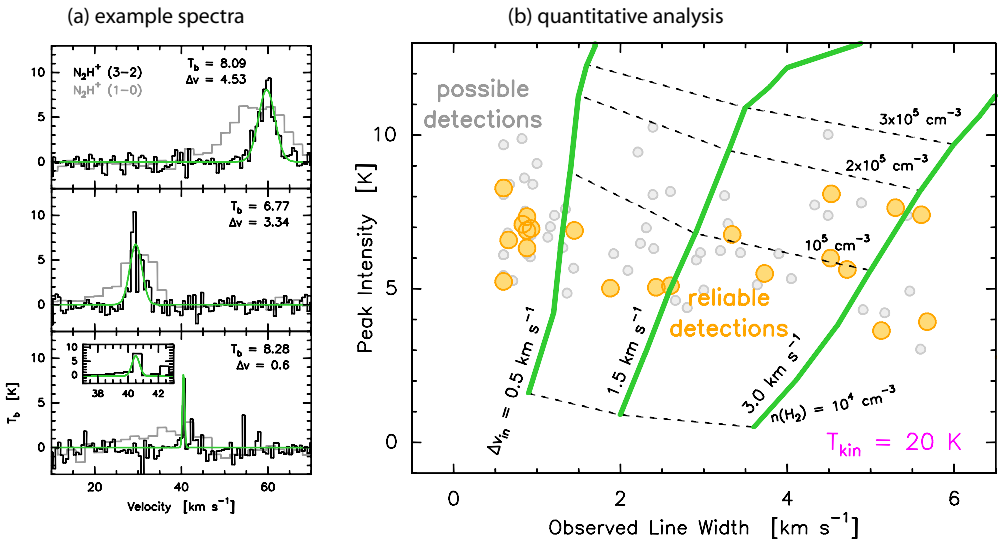

Figure 2. Analysis of SMA N_2H^+ (3–2) data. Panel (a) shows three bright reliable example spectra sampling the full range of observed velocity dispersions. CARMA N_2H^+ (1–0) spectra are overlaid for reference. Gaussian fits are summarized by green lines and fitted parameters. These fit results are analyzed in panel (b): possible and reliable detections are marked by gray and yellow circles, respectively. Model line widths and intensities, calculated with MOLLIE (Keto & Rybicki 2010) using a kinetic temperature of 20 K, are indicated (using green and dashed black lines, respectively) for a range of intrinsic line widths, $\Delta v_{\rm in}$, and densities at 0.1 pc radius, $n(H_2)$.

(A color version of this figure is available in the online journal.)

high-mass SF (HMSF) regions (Fontani et al. 2006; Zinchenko et al. 2009). Furthermore, all N_2H^+ cores show no significant dust emission. These cores are probably starless and have N_2H^+ abundances $\geqslant 10^{-9}$, as seen in IRDCs that are relatively dense and starless, resembling G0.253+0.016 (Ragan et al. 2006; Sakai et al. 2008; Vasyunina et al. 2011): for example, using MOLLIE to model cores with a higher N_2H^+ abundance of $\geqslant 10^{-9}$ and $\Delta v_{\rm in} = 1\,{\rm km\,s^{-1}}$, the predicted N_2H^+ (3–2) line intensity is $\geqslant$4.6 K, which is above the detection limit (Figure 2(b)), even when the density is $n_{0.1\,{\rm pc}} = 10^4\,{\rm cm^{-3}}$, which is an order of magnitude below that derived from the upper limit of the dust continuum flux ($<26\,M_\odot$ within 0.046 pc radius; Section 3.1).

3.3. CARMA Line Emission Maps: Many Fragments with Large Velocity Differences

Figure 3(d) shows maps for N_2H^+ (1–0) and SiO (2–1) observed with CARMA. The beam size is $7\farcs1 \times 3\farcs5$ (P.A. = 6°). We identify cloud fragments as continuous N_2H^+ (1–0) emission structures in position–position–velocity space exceeding an intensity threshold of 0.35 Jy beam^{-1} = 1.97 K (noise is 0.06–0.12 Jy beam^{-1}). These fragments, numbered 1–7, are shown in Figure 3(a). The threshold was chosen to yield a simple yet representative decomposition of the cloud structure. Segmentation was done using 3D Slicer[6] and CLUMPFIND (Williams et al. 1994), followed by manual removal of artifacts at map boundaries.

Fragment properties are listed in Table 1: from spectra integrated over each fragment, we calculate $\langle v \rangle$ and σ_v as the intensity-weighted velocity mean and standard deviation calculated directly from the velocities and intensities per channel, v_i and $T(v_i)$. Using intensity-weighted mean line-of-sight velocities calculated for every pixel, we also list the standard deviation among line-of-sight velocities within a given fragment, $\sigma_v^{\rm los}$. Velocity gradients, characterized by $\sigma_v^{\rm los}$, dominate the velocity dispersion, since $\sigma_v \approx \sigma_v^{\rm los}$. The effective radius, $R = (A/\pi)^{1/2}$, is calculated from the CLUMPFIND-derived fragment area within the 0.35 Jy beam^{-1} intensity surface, A.

Figure 3(b) illustrates that the SMA-detected N_2H^+ (3–2) cores are associated with the CARMA-detected N_2H^+ fragments, as expected for cores embedded in extended envelopes. Figure 3(c) demonstrates that the N_2H^+ fragments 4–7 are also detected in SiO.

Table 1
Fragment Properties

Fragment	$\langle v \rangle$ (km s^{-1})	σ_v (km s^{-1})	$\sigma_v^{\rm los}$ (km s^{-1})	R (pc)	α assuming 3×10^{23} cm^{-2}
1	−0.1	6.1	4.9	0.47	4.5
2	6.4	5.4	4.6	0.70	2.3
3	14.8	4.3	2.0	0.68	1.5
4	32.2	5.9	5.0	0.63	3.1
5	31.5	5.2	4.8	1.06	1.4
6	44.2	8.4	8.1	1.16	3.4
7	42.7	13.9	13.5	1.62	6.8

4. ANALYSIS

4.1. Star Formation Law

The most striking feature of G0.253+0.016, noted by all previous papers on the cloud, is its low SF rate. Here, we present the first quantitative comparison to recently proposed "SF laws."

Lada et al. (2010) suggest that molecular clouds typically contain one embedded YSO per $\sim 5\,M_\odot$ of gas at H_2 column densities $\geqslant 7 \times 10^{21}$ cm^{-2}. Since G0.253+0.016 contains $2 \times 10^5\,M_\odot$ at column densities $\geqslant 4.5 \times 10^{22}$ cm^{-2} (L12, plus correction in Section 3.1), the cloud should contain $\sim 4 \times 10^4$ YSOs.

[6] 3D Slicer is available from http://www.slicer.org. See http://am.iic.harvard.edu on astronomical research with 3D Slicer.

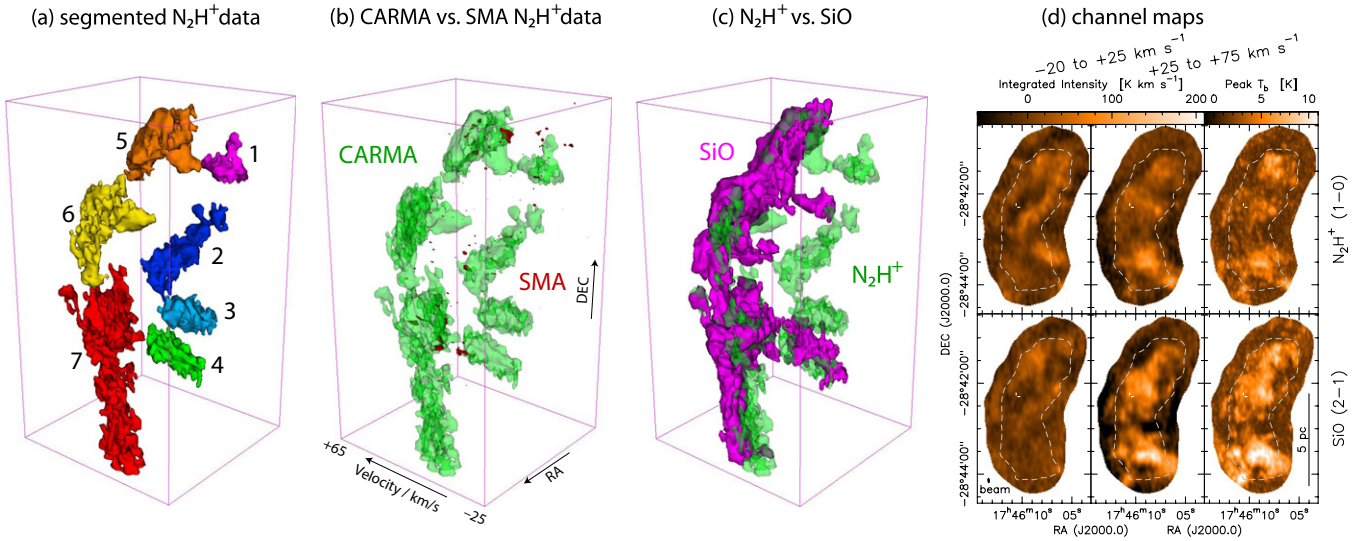

Figure 3. CARMA maps of G0.253+0.016. Panel (a) presents a cloud segmentation in position–position–velocity space. Panels (b) and (c) illustrate the complex velocity structure and chemistry (note discrepancy between SiO and N_2H^+). Panel (d) presents the same information, collapsed into two velocity ranges (left), and the peak spectral intensity per pixel (right). The dashed line is the lower SCUBA contour from Figure 1.

(A color version of this figure is available in the online journal.)

Lada et al. (2010) consider, of course, YSOs bright enough to be detected. We assume that Lada et al. cannot sense YSOs of mass $<0.08\,M_\odot$, and detect only 50% of stars with mass 0.08 to 0.5 $M_\odot$. For a typical stellar initial mass function (IMF), such as the $\alpha_3 = 2.7$ case of Kroupa (2002), the total number of stars down to 0.01 $M_\odot$ is equal to the Lada et al. YSO count times a factor 2.63.

Considering this IMF, a cluster of $\sim 4 \times 10^4$ YSOs similar to the sources considered by Lada et al. would contain stars of mass $\gtrsim 100\,M_\odot$. This contradicts radio continuum surveys for HII regions, ruling out stars with mass $\gtrsim 16\,M_\odot$ in G0.253+0.016 (Lis et al. 1994). Assuming a maximum stellar mass $\sim 16\,M_\odot$, the $\alpha_3 = 2.7$ Kroupa (2002) IMF, and the factor of 2.63 to account for YSOs too faint to be detected even in nearby clouds, the cloud should contain ~900 YSOs of the sort considered by Lada et al. (2010)—i.e., by a factor ~45 lesser than the $\sim 4 \times 10^4$ YSOs predicted by the Lada et al. (2010) law. See Lis et al. (2001) for a similar IMF analysis. The Lada et al. (2010) law thus does not provide a universal description of the SF process, contrary to assumptions by Lada et al. (2012) to explain the extragalactic Gao & Solomon (2004) infrared–HCN luminosity correlation.

4.2. Kinematics and Gravitational Binding

Stability against gravitational collapse can, e.g., be evaluated using the virial parameter, $\alpha = 5R\sigma_v^2/(GM)$ or

$$\alpha = 1.2 \left(\frac{\sigma_v}{\mathrm{km\,s^{-1}}}\right)^2 \left(\frac{R}{\mathrm{pc}}\right) \left(\frac{M}{10^3\,M_\odot}\right)^{-1}, \qquad (1)$$

where σ_v is the one-dimensional velocity dispersion and G is the constant of gravity. Slightly depending on the equation of state, collapse requires $\alpha \lesssim 2$ (Bertoldi & McKee 1992; Ebert 1955; Bonnor 1956).

L12 derive $M = 2.0 \times 10^5\,M_\odot$ within $R = 2.8$ pc (after correction in Section 3.1), and a line width $\Delta v = (8\,\ln[2])^{1/2}\,\sigma_v < 16\,\mathrm{km\,s^{-1}}$. This yields $\alpha < 0.8$: the cloud should collapse.

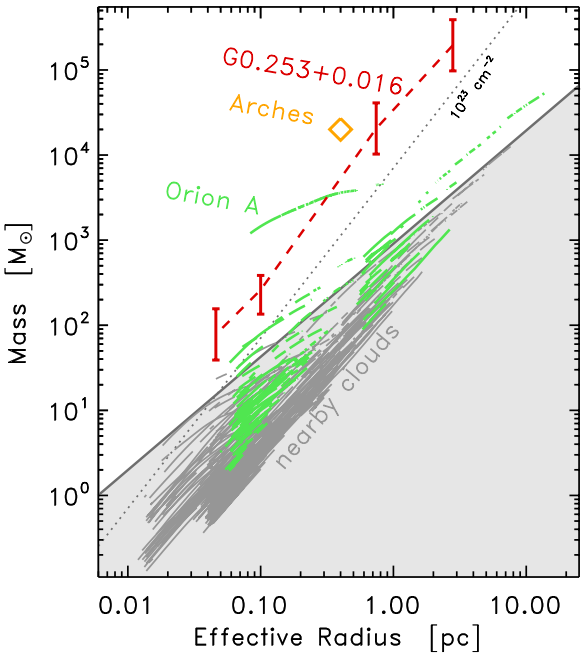

Figure 4. Density structure of G0.253+0.016 (red). Reference data are obtained using a hierarchical structure decomposition ("dendrograms": Rosolowsky et al. 2008), based on published structure analysis (Kauffmann et al. 2010a, 2010b; gray lines) and previously unexplored Orion A data (Kainulainen et al. 2011; see Section 4.3; green lines). For reference, the dotted line highlights an H_2 column density of $10^{23}\,\mathrm{cm^{-2}}$. The gray line and shading indicate the Kauffmann & Pillai (2010) limit (Equation (2)).

(A color version of this figure is available in the online journal.)

However, L12 exclude a component at $\approx 10\,\mathrm{km\,s^{-1}}$ radial velocity, which our maps show to be part of the cloud morphology (i.e., fragments 1–3; Figure 3). Inclusion of the $\approx 10\,\mathrm{km\,s^{-1}}$ component yields $\Delta v = (35 \pm 5)\,\mathrm{km\,s^{-1}}$ (Figure 4 of L12), resulting in $\alpha = 3.8^{+1.2}_{-1.0}$. G0.253+0.016 thus seems to be unbound. Fast motions $\Delta v > 16\,\mathrm{km\,s^{-1}}$ are also suggested by widespread SiO shocks (Section 4.5).

Still, many interferometer-detected structures seem to be bound. Using Equation (1), Table 1 reports α for CARMA-detected cloud fragments, assuming column densities $\sim 3 \times 10^{23}$ cm^{-2} (Section 4.3). For the SMA-detected N_2H^+ cores, we adopt $R = 0.1$ pc, and the density structure from Section 3.2. To include thermal pressure, we substitute $(\sigma_v^2 + [0.188\,\mathrm{km\,s^{-1}}]^2 \cdot [T_{\rm kin}/10\,\mathrm{K}])^{1/2}$ for σ_v in Equation (1). For $T_{\rm kin} \leqslant 80$ K, $\Delta v \leqslant 3.0$ km s^{-1}, and $n_{0.1\rm pc} = 10^5$ cm^{-3} (Figure 2), $\alpha \leqslant 1.8$ is obtained.

Many N_2H^+ (3–2) spectra reveal lines consistent with an intrinsic line width $\lesssim$0.5 km s^{-1} (Figure 2(b)). Compared with the $\gtrsim$10 km s^{-1} lines typically found in single-dish spectra of the GC region (e.g., Lis & Menten 1998), these are probably the most narrow lines detected so far in the GC region.

4.3. Density Structure

Figure 4 summarizes the density structure of G0.253+0.016. From L12, we take a mass of $2 \times 10^5\,M_\odot$ within 2.8 pc radius, and include their peak column density of 5.3×10^{23} cm^{-2} per 36″ beam at 0.7 pc radius ($1.7 \times 10^4\,M_\odot$; data scaled as explained in Section 3.1). Interferometer-based assessments ($78\,M_\odot$ and $[260 \pm 125]\,M_\odot$ at 0.046 and 0.1 pc radius, respectively) are from Sections 3.1 and 3.2. For dust-based measurements, we adopt an opacity-induced uncertainty by a factor two (Kauffmann et al. 2008). Reference data on non-HMSF clouds are from Kauffmann et al. (2010b). Unpublished Bolocam maps[7] (adopting 15 K dust temperature) and extinction data from Kainulainen et al. (2011) are used to characterize Orion A using methods from Kauffmann et al. (2010a; building on Rosolowsky et al. 2008). Espinoza et al. (2009) characterize the Arches cluster. An approximate mass-size limit for HMSF is taken from Kauffmann & Pillai (2010),

$$m_{\rm lim}(r) = 870\,M_\odot\,(r/\mathrm{pc})^{1.33}\,. \quad (2)$$

At $r = 2.8$ pc, G0.253+0.016 exceeds the mass of equal-sized structures in Orion A by a factor $\sim$25, and the Kauffmann & Pillai criterion by a factor 60. The mean H_2 volume and column densities are $M/(4/3\,\pi\,R^3) \rightarrow 3.2 \times 10^4$ cm^{-3} and 3.6×10^{23} cm^{-2}, respectively. However, at smaller spatial scales, G0.253+0.016 falls short of the masses of the Arches cluster and the most massive structures in Orion A by factors $\sim$4. At 0.046 pc radius, the Kauffmann & Pillai criterion is exceeded by a modest factor $\lesssim$5.

The interferometer-derived masses are probably underestimated. Note, e.g., that the peak column densities from SMA and *Herschel* data are similar, i.e., 5.2×10^{23} cm^{-2} vs. 5.3×10^{23} cm^{-2}. This may result from two factors. First, interferometer-induced spatial filtering may reduce observed intensities. Second, the dust opacity law might be different than assumed. None of this affects our conclusion that little dense gas exist in G0.253+0.016. For example, if masses were higher by a factor five, this would imply virial parameters $\alpha \leqslant 0.1$ for all SMA-detected N_2H^+ cores with line widths $\Delta v \sim 0.5$ km s^{-1}. Such low values for α are very unusual (T. Pillai et al., in preparation), and thus unlikely. This comparison suggests mass errors smaller than a factor five.

4.4. Decay of Gas Motions and Accretion onto Cores

HMSF in G0.253+0.016 is still possible if structures in the cloud grow more dense over time. Growth is controlled by the flow crossing time ℓ/σ_v for a spatial scale ℓ,

$$t_{\rm cross} = 1\,\mathrm{Myr}\left(\frac{\ell}{\mathrm{pc}}\right)\left(\frac{\sigma_v}{\mathrm{km\,s^{-1}}}\right)^{-1} \quad (3)$$

$$= 2.4\,\mathrm{Myr}\left(\frac{\ell}{\mathrm{pc}}\right)\left(\frac{\Delta v}{\mathrm{km\,s^{-1}}}\right)^{-1}. \quad (4)$$

For the entire cloud, using $\ell = 2R$ and $\Delta v \approx 35$ km s^{-1}, $t_{\rm cross} \approx 0.4$ Myr. Undriven turbulence is expected to decay as $e^{-t/t_{\rm cross}}$ (Mac Low & Klessen 2004). Thus, global collapse would take several 0.4 Myr.

If the observed velocity dispersions were reflecting pure inward motions of speed $\sigma_v/2$, structures of constant radius R could ingest material from radii $r = R$ to $2R$ within the time $(2R - R)/(\sigma_v/2) = 2R/\sigma_v \equiv 2 \cdot t_{\rm cross}$. For the N_2H^+ fragments listed in Table 1, $2R/\sigma_v = 0.14$ to 0.40 Myr. Adopting $R = 0.1$ pc and $\Delta v = 0.5$ to 6.0 km s^{-1} (Figure 2), $2R/\sigma_v = 0.08$–0.9 Myr holds for the SMA-detected structures.

These timescales control the structure evolution. Several 10^5 yr must pass before cores as dense as those in Orion A can form.

4.5. Nature and Future of G0.253+0.016

The low SF rate for this compact and massive cloud indicates that G0.253+0.016 is in an extreme physical state (Section 4.1). Lis & Menten (1998) and Lis et al. (2001) take the existence of widespread SiO emission as evidence for an ongoing cloud–cloud collision. This molecule is believed to trace shocks unambiguously: silicon is usually locked up in dust grains and requires grain–grain collisions at velocities $\gtrsim$20 km s^{-1} to be released (Guillet et al. 2009). Further gas-phase reactions yield SiO in $\lesssim 10^3$ yr. Figure 3 shows for the first time that the SiO distribution is likely too smooth and extended to result from outflows associated with a population of embedded stars. Processes on larger spatial scales, such as cloud–cloud collisions, are a more probable origin. It thus seems plausible that G0.253+0.016 is a very young cloud that will soon dissipate internal motions and efficiently form stars in a few 10^5 yr (Section 4.4).

However, the cloud may not be gravitationally bound and simply disperse (Section 4.2). Furthermore, G0.253+0.016 is subject to the disruptive GC environment: as already mentioned by L12, following the GC orbit proposed by Molinari et al. (2011), G0.253+0.016 will arrive at the present location of Sgr B2 in $\sim 8.5 \times 10^5$ yr. The latter cloud essentially represents a standing shock, where gas clouds on different GC orbit families collide (e.g., Bally et al. 2010). Given the disturbed nature of the Sgr B2 region, it is not clear whether G0.253+0.016 will then be disrupted or be pushed into collapse.

5. CONCLUSION

G0.253+0.016 deviates from current "star formation laws" (e.g., Lada et al. 2010) by a factor $\sim$45 (Section 4.1). The scarcity of significant dust and N_2H^+ cores in our SMA interferometer maps (Sections 3.1 and 3.2) reveals that G0.253+0.016 is presently far away from forming high-mass stars and clusters (Section 4.3): considerable evolution for several 10^5 yr is needed before such star formation might occur (Section 4.4). The cloud might thus be very young and currently forming in a cloud–cloud collision indicated by SiO shocks (Section 4.5). Given the disruptive dynamics of the galactic center region (Section 4.5), and

[7] We are indebted to D. Li for providing the data, and A. Ginsburg for reducing it.

the potentially unbound nature of the cloud (Section 4.2), it is unclear whether evolution toward significant star formation will ever happen.

We thank S. Longmore for giving us access to Longmore et al. (2012) in advance of publication, D. Lis and K. Menten for enlightening discussions, and the anonymous referee for making the Letter more readable. J.K. is grateful to D. Li and P. Goldsmith, his hosts at JPL, for making this work possible. Part of the research was carried out at the Jet Propulsion Laboratory, California Institute of Technology, under a contract with the National Aeronautics and Space Administration. T.P. acknowledges support from CARMA, which is supported by the National Science Foundation through grant AST 05–40399. J.K. acknowledges support from Dewey, Cheetham & Howe (Cambridge, MA).

Facilities: SMA, CARMA, Spitzer

REFERENCES

Bally, J., Aguirre, J., Battersby, C., et al. 2010, ApJ, 721, 137
Bertoldi, F., & McKee, C. F. 1992, ApJ, 395, 140
Bonnor, W. 1956, MNRAS, 116, 351
Carey, S. J., Clark, F. O., Egan, M. P., et al. 1998, ApJ, 508, 721
Caswell, J. L., Breen, S. L., & Ellingsen, S. P. 2011, MNRAS, 410, 1283
Caswell, J. L., Fuller, G. A., Green, J. A., et al. 2010, MNRAS, 404, 1029
Di Francesco, J., Johnstone, D., Kirk, H., MacKenzie, T., & Ledwosinska, E. 2008, ApJS, 175, 277
Ebert, R. 1955, ZA, 37, 217
Espinoza, P., Selman, F. J., & Melnick, J. 2009, A&A, 501, 563
Fontani, F., Caselli, P., Crapsi, A., et al. 2006, A&A, 460, 709
Gao, Y., & Solomon, P. M. 2004, ApJ, 606, 271
Guesten, R., Walmsley, C. M., & Pauls, T. 1981, A&A, 103, 197
Guillet, V., Jones, A. P., & Pineau des Forêts, G. 2009, A&A, 497, 145
Gutermuth, R. A., Pipher, J. L., Megeath, S. T., et al. 2011, ApJ, 739, 84
Heiderman, A., Evans, N. J., Allen, L. E., Huard, T., & Heyer, M. 2010, ApJ, 723, 1019
Kainulainen, J., Beuther, H., Banerjee, R., Federrath, C., & Henning, T. 2011, A&A, 530, A64
Kauffmann, J., Bertoldi, F., Bourke, T. L., Evans, N. J., & Lee, C. W. 2008, A&A, 487, 993
Kauffmann, J., & Pillai, T. 2010, ApJL, 723, L7
Kauffmann, J., Pillai, T., Shetty, R., Myers, P. C., & Goodman, A. A. 2010a, ApJ, 712, 1137
Kauffmann, J., Pillai, T., Shetty, R., Myers, P. C., & Goodman, A. A. 2010b, ApJ, 716, 433
Kennicutt, R. C. J., & Evans, N. J. I. 2012, ARA&A, 50, 531
Keto, E., & Rybicki, G. 2010, ApJ, 716, 1315
Kroupa, P. 2002, Sci, 295, 82
Lada, C. J., Forbrich, J., Lombardi, M., & Alves, J. a. F. 2012, ApJ, 745, 190
Lada, C. J., Lombardi, M., & Alves, J. a. F. 2010, ApJ, 724, 687
Lis, D. C., & Menten, K. M. 1998, ApJ, 507, 794
Lis, D. C., Menten, K. M., Serabyn, E., & Zylka, R. 1994, ApJL, 423, L39
Lis, D. C., Serabyn, E., Zylka, R., & Li, Y. 2001, ApJ, 550, 761
Longmore, S. N., Rathborne, J., Bastian, N., et al. 2012, ApJ, 746, 117
Mac Low, M.-M., & Klessen, R. 2004, RvMP, 76, 125
Molinari, S., Bally, J., Noriega-Crespo, A., et al. 2011, ApJL, 735, L33
Ossenkopf, V., & Henning, T. 1994, A&A, 291, 943
Pillai, T., Kauffmann, J., Wyrowski, F., et al. 2011, A&A, 530, A118
Ragan, S. E., Bergin, E. A., Plume, R., et al. 2006, ApJS, 166, 567
Rosolowsky, E., Pineda, J., Kauffmann, J., & Goodman, A. 2008, ApJ, 679, 1338
Sakai, T., Sakai, N., Kamegai, K., et al. 2008, ApJ, 678, 1049
Tafalla, M., Santiago-García, J., Myers, P. C., et al. 2006, A&A, 455, 577
Vasyunina, T., Linz, H., Henning, T., et al. 2011, A&A, 527, A88
Williams, J., de Geus, E., & Blitz, L. 1994, ApJ, 428, 693
Wu, J., Evans, N. J., Shirley, Y. L., & Knez, C. 2010, ApJS, 188, 313
Zhang, Q., Wang, Y., Pillai, T., & Rathborne, J. 2009, ApJ, 696, 268
Zinchenko, I., Caselli, P., & Pirogov, L. 2009, MNRAS, 395, 2234